

Time-domain solver in curvilinear coordinates for outdoor sound propagation over complex terrain

Didier Dagna^{a)} and Philippe Blanc-Benon

Laboratoire de Mécanique des Fluides et d'Acoustique, Unité Mixte de Recherche CNRS 5509,
École Centrale de Lyon, Université de Lyon, 36, Avenue Guy de Collongue, 69134 Écully Cedex, France

Franck Poisson

Société Nationale des Chemins de fer Français, 40, Avenue des Terroirs de France, 75611 Paris Cedex 12,
France

(Received 8 January 2013; revised 12 April 2013; accepted 12 April 2013)

The current work aims at developing a linearized Euler equations solver in curvilinear coordinates to account for the effects of topography on sound propagation. In applications for transportation noise, the propagation environment as well as the description of acoustic sources is complex, and time-domain methods have proved their capability to deal with both atmospheric and ground effects. First, equations in curvilinear coordinates are examined. Then time-domain boundary conditions initially proposed for a Cartesian coordinate system are implemented in the curvilinear solver. Two test cases dealing with acoustic scattering by an impedance cylinder in a two-dimensional geometry and by an impedance sphere in a three-dimensional geometry are considered to validate the boundary conditions. Accurate solutions are obtained for both rigid and impedance surfaces. Finally, the solver is used to examine a typical outdoor sound propagation problem. It is shown that it is well-suited to study coupled effects of topography, mixed impedance ground and meteorological conditions.

© 2013 Acoustical Society of America. [<http://dx.doi.org/10.1121/1.4803863>]

PACS number(s): 43.28.Js, 43.28.En, 43.50.Vt, 43.20.El [VEO]

Pages: 3751–3763

I. INTRODUCTION

Time-domain methods are attractive to study broadband noise propagation in outdoor environments. Indeed, they allow consideration of complex situations and especially realistic meteorological conditions. They have been used extensively for the past 10 years for this purpose (Blumrich and Heimann, 2002; Van Renterghem and Botteldooren, 2003; Ostashev *et al.*, 2005; Hornikx *et al.*, 2010; Guillaume *et al.*, 2011). Modeling of ground interactions is more challenging because it is essentially a frequency-dependent phenomenon. Thus time-domain counterparts must verify some physical laws, such as causality (see e.g., Rienstra, 1988), and can require time-demanding operations, such as computation of convolution (see, e.g., Özyörük and Long, 1996). Two main approaches are developed in the literature to account for ground interactions, one that relies on the computation of the acoustic waves propagation in the ground layer (Salomons *et al.*, 2002; Wilson *et al.*, 2007), and one that is based on the more or less direct translation of the impedance boundary condition from the frequency domain to the time domain (Ostashev *et al.*, 2007). Following the latter, Cotté *et al.* (2009) have proposed a time-domain impedance boundary condition for locally reacting surfaces, based on a recursive convolution technique, and have shown that it was numerically efficient. It has been implemented in a solver using high-order finite-difference techniques and has been used to study long range propagation over an impedance flat

ground (Dagna *et al.*, 2011). In particular, acoustic surface waves have been exhibited.

This paper aims to go a step further in modeling realistic outdoor sound propagation problems by introducing effects of topography. In the literature, many techniques have been proposed to account for topography. Among wave-based approaches, parabolic equation methods have been the object of a lot of studies. In Sack and West (1995), a coordinate transformation adapted for a given ground profile is performed in the Helmholtz equation, and a one-way wave equation is derived from the obtained expression. To our knowledge, this technique has not been applied to more complex propagation equations, using parabolic equation techniques, to accurately handle wind gradients. An other approach, initially introduced by Collins (1990) in underwater acoustics, and applied by Blairon *et al.* (2002) to outdoor sound propagation problems, allows to deal with complex meteorological conditions. The main idea of that approach is to approximate the ground profile by line segments. At each slope break, a rotation of the numerical domain is performed, and the parabolic equation is then solved on a Cartesian mesh. This technique has been validated against acoustic pressure measurements done in Saint-Berthevin in France in 2002 (Lihoreau *et al.*, 2006). More recently, Parakkal *et al.* (Parakkal *et al.*, 2010; Parakkal *et al.*, 2012) have proposed two different techniques to treat non-flat grounds by parabolic equation methods. In the paper published in 2010, a generalized polar coordinate method adapted to propagation over large-scale terrain features is proposed, and model's prediction compares favorably to experimental data. In their second paper, they introduced the Beilis–Tappert parabolic equation method into the outdoor

^{a)}Author to whom correspondence should be addressed. Electronic mail: didier.dagna@ec-lyon.fr

sound propagation community. This method has been successfully used in electromagnetic propagation and underwater acoustic (Jensen *et al.*, 1994) but is limited for now to surface slopes up to 20°. In time-domain methods, Heimann and Karle (2006) have used a similar approach to that of Sack and West. In their study, different terrain-following coordinate transformations for the linearized Euler equations are examined, and ground effect is accounted for by solving propagation equations in the ground layer. Among other popular methods, boundary element methods are probably the best suited to treat propagation over non-flat ground surfaces (see, e.g., Jean, 1998). These methods require knowledge of the Green's function. They can be applied to acoustic propagation in an inhomogeneous medium with a constant sound-speed gradient (Premat and Gabillet, 2000), but complex meteorological effects, such as scattering by atmospheric turbulence, can not be properly accounted for.

In this paper, following the ideas used for aeroacoustics problems (see, e.g., Marsden *et al.*, 2005), a time-domain solver in curvilinear coordinates is developed to treat acoustic propagation over complex ground profiles. Curvilinear transformation is a more general approach to that proposed by Heimann and Karle (2006) because any continuous coordinate transformation can be considered. The time-domain impedance boundary condition of Cotté *et al.* (2009) is extended to this case. Possible applications are acoustic propagation in a non-homogeneous atmosphere and over a complex site with a realistic topography and with mixed impedance ground.

The paper is organized as follows. In Sec. II, the propagation solver is described. The time-domain boundary condition in curvilinear coordinates for a rigid ground and for an impedance ground is then presented. In Sec. III, two test cases for two- and three-dimensional (2-D and 3-D) geometries including diffraction of acoustic waves are considered to validate the proposed method. Last, in Sec. IV, propagation of acoustic waves over a 3-D embankment is studied with different meteorological conditions to illustrate the possibilities of the solver.

II. SOLVER OF THE LINEARIZED EULER EQUATIONS IN THE CURVILINEAR COORDINATES

In this study, sound propagation in the atmosphere is described by a set of coupled equations for the acoustic pressure p and the acoustic velocity $\mathbf{v} = (v_x, v_y, v_z)$, given in the physical domain (x, y, z) by

$$\frac{\partial p}{\partial t} + (\mathbf{V}_0 \cdot \nabla)p + \rho_0 c^2 \nabla \cdot \mathbf{v} = \rho_0 c^2 Q, \quad (1)$$

$$\rho_0 \frac{\partial \mathbf{v}}{\partial t} + \rho_0 (\mathbf{V}_0 \cdot \nabla) \mathbf{v} + \rho_0 (\mathbf{v} \cdot \nabla) \mathbf{V}_0 + \nabla p = \mathbf{R}, \quad (2)$$

where $\mathbf{V}_0 = (V_{0x}, V_{0y}, V_{0z})$ is the mean flow, ρ_0 is the mean density of air, and c is the adiabatic sound speed in the air. The preceding equations correspond to the linearized Euler equations (LEEs) where terms of order $(|\mathbf{V}_0|/c)^2$ are omitted. Their derivation is presented in Ostashev *et al.* (2005). In the examples presented in this study, the sound speed is

constant, $c = c_0$, where c_0 is the reference sound speed. The source terms Q and \mathbf{R} represent, respectively, a mass source and external forces. The linearized Euler equations are then written in the following conservative form:

$$\frac{\partial \mathbf{U}}{\partial t} + \frac{\partial \mathbf{E}}{\partial x} + \frac{\partial \mathbf{F}}{\partial y} + \frac{\partial \mathbf{G}}{\partial z} + \mathbf{H} = \mathbf{S}, \quad (3)$$

where $\mathbf{U} = [p, \rho_0 v_x, \rho_0 v_y, \rho_0 v_z]^T$ is the unknown vector, \mathbf{E} , \mathbf{F} , \mathbf{G} , and \mathbf{H} are the Eulerian fluxes, and \mathbf{S} is the source vector.

A. Curvilinear equations

Low-dissipation and low-dispersion techniques are required to obtain accurate numerical solutions in long range sound propagation problems. They are generally applied to a Cartesian mesh. Thus a special treatment is needed to account for non-flat boundaries. Extrapolation methods have been proposed in the literature (Kurbatskii and Tam, 1997). However, they can suffer from numerical instabilities, and the implementation of boundary conditions remains complex. These issues are overcome by using curvilinear coordinates (Marsden *et al.*, 2005). The idea is to define a mapping from a Cartesian mesh to a curvilinear mesh that fits accurately the boundary. Thus the numerical methods developed for Cartesian meshes can still be used. The principle of the method is illustrated in Fig. 1.

Let us consider that the Cartesian coordinates are functions of the curvilinear coordinates (ξ, ζ, η) , i.e., $x = x(\xi, \zeta, \eta)$, $y = y(\xi, \zeta, \eta)$, and $z = z(\xi, \zeta, \eta)$. To get the LEEs in the transformed system, chain rule expansions are used,

$$\left[\frac{\partial}{\partial x} \frac{\partial}{\partial y} \frac{\partial}{\partial z} \right]^T = \mathbf{J} \left[\frac{\partial}{\partial \xi} \frac{\partial}{\partial \zeta} \frac{\partial}{\partial \eta} \right]^T, \quad (4)$$

where $\mathbf{J} = \partial(\xi, \zeta, \eta)/\partial(x, y, z)$ is the Jacobian matrix of the transformation. The equations are then written in the conservative form

$$\frac{\partial \mathbf{U}^*}{\partial t} + \frac{\partial \mathbf{E}^*}{\partial \xi} + \frac{\partial \mathbf{F}^*}{\partial \zeta} + \frac{\partial \mathbf{G}^*}{\partial \eta} + \mathbf{H}^* = \mathbf{S}^*, \quad (5)$$

where the fluxes are

$$\mathbf{U}^* = \mathbf{U}/J, \quad (6)$$

$$\mathbf{E}^* = (\xi_x \mathbf{E} + \xi_y \mathbf{F} + \xi_z \mathbf{G})/J, \quad (7)$$

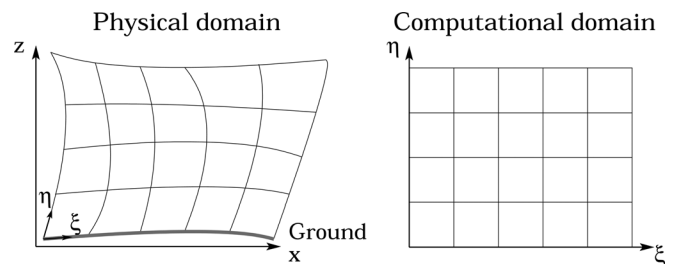


FIG. 1. Coordinate transformation from the physical domain (x, z) to the computational domain (ξ, η) .

$$\mathbf{F}^* = (\zeta_x \mathbf{E} + \zeta_y \mathbf{F} + \zeta_z \mathbf{G})/J, \quad (8)$$

$$\mathbf{G}^* = (\eta_x \mathbf{E} + \eta_y \mathbf{F} + \eta_z \mathbf{G})/J, \quad (9)$$

$$\mathbf{H}^* = \mathbf{H}/J, \quad (10)$$

$$\mathbf{S}^* = \mathbf{S}/J. \quad (11)$$

In the preceding equations, $J = |\mathbf{J}|$ is the Jacobian of the transformation. The notation $i_j = \partial i / \partial j$ is employed to express the partial derivatives of the coordinate functions.

B. Numerical aspects

The linearized Euler equations in curvilinear coordinates in Eq. (5) are solved by using low-dispersive and low-dissipative numerical schemes developed in the computational aeroacoustics community. Optimized finite-difference schemes and selective filters over 11 points are used to compute the spatial derivative and to remove grid-to-grid oscillations, respectively and allow accurate computation of acoustic wavelengths down to five or six times the spatial mesh size. For the interior points, the centered fourth-order finite-difference scheme of [Bogey and Bailly \(2004\)](#) and the sixth-order selective filter of [Bogey et al. \(2009\)](#) are chosen. For the boundary points, the non-centered finite-difference schemes and the non-centered selective filters of [Berland et al. \(2007\)](#) are used. Applying a selective filter over $P + Q + 1$ points to a variable U on a uniform mesh of size Δx gives

$$U^f(x_0) = U(x_0) - \sigma_f \sum_{m=-P}^Q d_m U(x_0 + m\Delta x), \quad (12)$$

where U^f is the filtered variable and d_m are the stencil coefficients. The filtering coefficient σ_f is set to 0.2 for all filters except at the end points at which the filtering coefficient is 0.01. The time integration is performed with the six-step fourth-order Runge–Kutta algorithm of [Berland et al. \(2006\)](#) called RK46-L.

The time-domain boundary conditions described in the next subsection are applied at the ground. At the outer boundaries, the radiation boundary conditions developed by [Tam and Dong \(1996\)](#) for 2-D cases and its extension proposed by [Bogey and Bailly \(2002\)](#) for 3-D cases are used. They are based on an asymptotic solution of the LEEs in free-field. A reference point must be chosen to define the far-field formulation. It must be close to the acoustic sources and sufficiently far from the outer boundaries, so that the far-field approximation is valid. Otherwise, as shown by [Mesbah et al. \(2008\)](#), noticeable reflecting waves can be generated at the nonreflecting boundaries. These radiation boundary conditions have been used successfully in outdoor sound propagation problems by [Cotté et al. \(2009\)](#) and [Dragna et al. \(2011\)](#).

A numerical study on the accuracy of the curvilinear transformation using the finite-difference schemes presented in the preceding text has been performed by [Marsden \(2005\)](#). It has been shown that a single mesh cell can be distorted up to 50° without leading to noticeable errors. This

gives a limit value for the slope angle, using a terrain-following coordinate transformation. Moreover, errors induced by the deformation of a computational molecule, i.e., the entire points in the stencil of the finite-difference scheme, remain negligible for deformation angle up to 100° . This shows that curvilinear coordinates transformations allow to consider larger slope angles than terrain-following coordinate transformations.

Only the transformation $(x(\xi, \zeta, \eta), y(\xi, \zeta, \eta), z(\xi, \zeta, \eta))$ is known *a priori*. Therefore at the beginning of the computation, the coefficients of the Jacobian matrix that appear in the expression of the Eulerian fluxes [see Eqs. (6) to (11)] must be computed. These coefficients must verify the geometric conservation laws (GCLs), that are given for a non-moving grid by (see, e.g., [Visbal and Gaitonde, 2002](#))

$$\left(\frac{\xi_x}{J}\right)_\xi + \left(\frac{\zeta_x}{J}\right)_\zeta + \left(\frac{\eta_x}{J}\right)_\eta = 0, \quad (13)$$

$$\left(\frac{\xi_y}{J}\right)_\xi + \left(\frac{\zeta_y}{J}\right)_\zeta + \left(\frac{\eta_y}{J}\right)_\eta = 0, \quad (14)$$

$$\left(\frac{\xi_z}{J}\right)_\xi + \left(\frac{\zeta_z}{J}\right)_\zeta + \left(\frac{\eta_z}{J}\right)_\eta = 0. \quad (15)$$

These laws have been implicitly invoked when going from Eq. (3) to Eq. (5). The GCLs are formally satisfied but they could be violated numerically for 3-D problems due to discretization, which can lead to severe errors ([Visbal and Gaitonde, 2002](#)). To avoid these difficulties, the metric coefficients are computed using the conservative form proposed by [Vinokur and Yee \(2000\)](#). For instance, the first metric coefficient is computed using

$$\xi_x = \frac{J}{2} [(y_\zeta z - z_\zeta y)_\eta - (y_\eta z - z_\eta y)_\zeta]. \quad (16)$$

Other equations follow from a cyclic permutation of (x, y, z) and (ξ, ζ, η) .

C. Time-domain boundary condition

Sound propagation over natural ground can be generally reduced to that over impedance surfaces using the so-called local reaction approximation (see, e.g., [Attenborough, 2002](#)). The boundary impedance condition is classically written in the frequency domain as $P(\omega) + Z(\omega)V_n(\omega) = 0$, where ω is the angular frequency, and P and V_n are the Fourier transforms of the pressure p and of the acoustic velocity normal to the ground v_n . Note that the normal to the ground surface points out of the ground. For a rigid ground, $v_n = 0$ and the surface impedance is infinite. In the time domain, the impedance boundary condition leads to a convolution

$$p(t) = - \int_{-\infty}^t z(t-t')v_n(t')dt', \quad (17)$$

where $z(t)$ is the inverse Fourier transform of the impedance. Not all surface impedance models are physically possible. As discussed by [Rienstra \(1988\)](#), $z(t)$ must be causal and

real. Moreover, because the ground absorbs energy, one must have $\text{Re}[Z(\omega)] > 0$, for $\omega > 0$, where Re denotes the real part. When solving Eq. (5), the components of the acoustic velocity are computed in the Cartesian system $(\mathbf{e}_x, \mathbf{e}_y, \mathbf{e}_z)$. It is then necessary to define a local coordinate system to calculate the components of the acoustic velocity normal and tangential to the ground surface. Without loss of generality, the ground surface corresponds in this study to the plane $\eta = 0$. Therefore the unitary normal vector is the third contravariant base vector

$$\mathbf{e}^\eta = \nabla \eta / |\nabla \eta|, \quad (18)$$

with $\nabla \eta = \eta_x \mathbf{e}_x + \eta_y \mathbf{e}_y + \eta_z \mathbf{e}_z$. The unitary vectors tangent to the ground surface are chosen as the two first covariant base vectors

$$\mathbf{e}_\xi = \nabla_\xi / |\nabla_\xi| \text{ and } \mathbf{e}_\zeta = \nabla_\zeta / |\nabla_\zeta|, \quad (19)$$

with $\nabla_\xi = x_\xi \mathbf{e}_x + y_\xi \mathbf{e}_y + z_\xi \mathbf{e}_z$ and $\nabla_\zeta = x_\zeta \mathbf{e}_x + y_\zeta \mathbf{e}_y + z_\zeta \mathbf{e}_z$. The vectors \mathbf{e}_ξ and \mathbf{e}_ζ are directed along the ξ and ζ lines, respectively. Note that the coordinate system $(\mathbf{e}_\xi, \mathbf{e}_\zeta, \mathbf{e}^\eta)$ is orthogonal only if the mesh is orthogonal at the ground surface. A scheme representing the two coordinate systems is depicted in Fig. 2.

The acoustic velocity can be expressed as $\mathbf{v} = v_x \mathbf{e}_x + v_y \mathbf{e}_y + v_z \mathbf{e}_z = v_\xi \mathbf{e}_\xi + v_\zeta \mathbf{e}_\zeta + v_n \mathbf{e}^\eta$. Thus the components of \mathbf{v} in the coordinate system $(\mathbf{e}_\xi, \mathbf{e}_\zeta, \mathbf{e}^\eta)$ are calculated with

$$v_n = \frac{\eta_x v_x + \eta_y v_y + \eta_z v_z}{|\nabla \eta|}, \quad (20)$$

$$v_\xi = \frac{x_\xi v_x + y_\xi v_y + z_\xi v_z}{|\nabla_\xi| (1 - \mathbf{e}_\xi \cdot \mathbf{e}_\xi^2)} - \mathbf{e}_\xi \cdot \mathbf{e}_\zeta \frac{x_\zeta v_x + y_\zeta v_y + z_\zeta v_z}{|\nabla_\zeta| (1 - \mathbf{e}_\zeta \cdot \mathbf{e}_\zeta^2)}, \quad (21)$$

$$v_\zeta = \frac{x_\zeta v_x + y_\zeta v_y + z_\zeta v_z}{|\nabla_\zeta| (1 - \mathbf{e}_\zeta \cdot \mathbf{e}_\zeta^2)} - \mathbf{e}_\zeta \cdot \mathbf{e}_\xi \frac{x_\xi v_x + y_\xi v_y + z_\xi v_z}{|\nabla_\xi| (1 - \mathbf{e}_\xi \cdot \mathbf{e}_\xi^2)}. \quad (22)$$

For an orthogonal system, the scalar product $\mathbf{e}_\xi \cdot \mathbf{e}_\zeta$ is null, and the preceding equations are greatly simplified. Similarly, the components of \mathbf{v} in the Cartesian coordinates system are retrieved with the relations

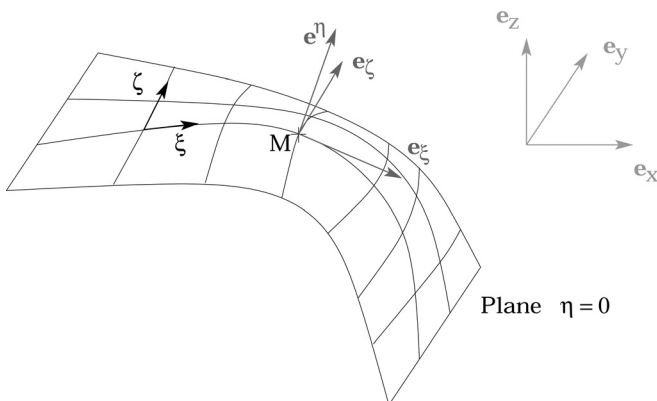


FIG. 2. Ground surface and definition of the coordinate systems.

$$v_x = \frac{\eta_x}{|\nabla \eta|} v_n + \frac{x_\xi}{|\nabla_\xi|} v_\xi + \frac{x_\zeta}{|\nabla_\zeta|} v_\zeta, \quad (23)$$

$$v_y = \frac{\eta_y}{|\nabla \eta|} v_n + \frac{y_\xi}{|\nabla_\xi|} v_\xi + \frac{y_\zeta}{|\nabla_\zeta|} v_\zeta, \quad (24)$$

$$v_z = \frac{\eta_z}{|\nabla \eta|} v_n + \frac{z_\xi}{|\nabla_\xi|} v_\xi + \frac{z_\zeta}{|\nabla_\zeta|} v_\zeta. \quad (25)$$

1. Rigid ground

At a rigid ground, the normal velocity v_n is equal to zero. Let us denote by $p^{(m)}$ and $\mathbf{v}^{(m)}$ the values of pressure and acoustic velocity at the discretized time $m\Delta t$. The following time marching is applied:

1. Advance in time the pressure and the components of acoustic velocity to get $p^{(m)}$ and $\mathbf{v}^{(m)}$ over the computational domain,
2. Compute v_ξ and v_ζ at the ground [see Eqs. (21) and (22)],
3. Impose v_x , v_y , and v_z at the ground by setting $v_n = 0$ in Eqs. (23) to (25).

2. Impedance ground

To account for impedance ground surfaces, we use in this study a time-domain boundary-condition (TDBC) derived by Reymen *et al.* (2006) on the basis of work done in electromagnetism (Luebbers and Hunsberger, 1992). This TDBC has been introduced in outdoor sound propagation community by Cotté *et al.* (2009) and is general in that it is not based on any impedance model. The TDBC requires the approximation of the impedance in the frequency-domain by a rational function

$$Z(\omega) \approx Z_\infty + \sum_{k=1}^N \frac{A_k}{\lambda_k - i\omega}, \quad (26)$$

where Z_∞ is the limit value of $Z(\omega)$ as ω tends to infinite, λ_k are the poles, N is the number of poles, and A_k are numerical coefficients. The causality condition is verified for this type of impedance model if and only if the real parts of λ_k are positive (Reymen *et al.*, 2006). The condition $\text{Re}[Z(\omega)] > 0$ for $\omega > 0$ must be checked for each set of coefficients (A_k, λ_k) . Because the inverse Fourier transform of the impedance in Eq. (26),

$$z(t) = Z_\infty \delta(t) + \sum_{k=1}^N A_k e^{-\lambda_k t} \mathbf{H}(t), \quad (27)$$

must be real (see, e.g., Rienstra, 1988), the poles λ_k are real or complex conjugates. In the preceding equation, $\mathbf{H}(t)$ is the Heaviside function. The derivation of the TDBC is detailed in Reymen *et al.* (2006) for both real and complex conjugates poles. The impedance models used in this study are appropriately approximated over the frequency bandwidth of interest by rational functions with real poles. Therefore we only present the TDBC for real poles. Different methods are proposed in Cotté *et al.* (2009) to determine the coefficients

λ_k and A_k . After inserting the formula for the impedance in Eq. (27) into Eq. (17), a recursive convolution method can be applied. Assuming that the normal velocity is constant over a time step, the following relation between $p^{(m)}$ and $v_n^{(m)}$ is obtained

$$p^{(m)} = -Z_\infty v_n^{(m)} + \sum_{k=1}^N A_k \phi_k^{(m)}, \quad (28)$$

where $\phi_k^{(m)}$ are called the accumulators. They are computed by the recursive expression

$$\phi_k^{(m)} = -v_n^{(m)} \frac{1 - e^{-\lambda_k \Delta t}}{\lambda_k} + \phi_k^{(m-1)} e^{-\lambda_k \Delta t}. \quad (29)$$

The TDBC relates the acoustic pressure to the normal velocity at the ground surface. One can then impose either p or v_n . Because it is easier to consider a scalar quantity than a vector quantity, we choose here to impose the pressure at the boundary. However, note that the implementation based on the acoustic velocity is feasible and does not lead to particular numerical problems. The following time-marching is then proposed:

1. Advance in time the pressure and the components of acoustic velocity to get $p^{(m)}$ and $\mathbf{v}^{(m)}$ over the computational domain,
2. Compute v_n at the ground with Eq. (20),
3. Advance in time the accumulators with Eq. (29),
4. Impose p at the ground with Eq. (28).

III. TEST CASES

Scattering problems are studied as test cases to demonstrate the accuracy of the boundary conditions treatment proposed in the previous section. The 2-D case, corresponding to scattering by an impedance cylinder, is based on the second problem in category 1 proposed in the Second Computational Aeroacoustics Workshop on Benchmark Problems (Tam and Hardin, 1997). In the initial benchmark, the cylinder is rigid. In this study, the test case is extended to impedance cylinders. The 3-D case corresponds to scattering by an impedance sphere and is a direct extension of the 2-D case. The schematic of the problem is depicted in Fig. 3. Dimensionless variables are used, with the following scales:

- Length scale: R ,
- Velocity scale: c_0 ,
- Time scale: R/c_0 ,
- Density scale: ρ_0 ,
- Pressure scale: $\rho_0 c_0^2$,
- Impedance scale: $\rho_0 c_0$,
- Air flow resistivity scale: $\rho_0 c_0 / R$,

where R is the radius of the cylinder (2-D case) or of the sphere (3-D case).

In the test cases, the impedance model is chosen as the Miki impedance model (Miki, 1990) of a rigidly backed layer of thickness d_L and of air flow resistivity σ_0 , given by the formula

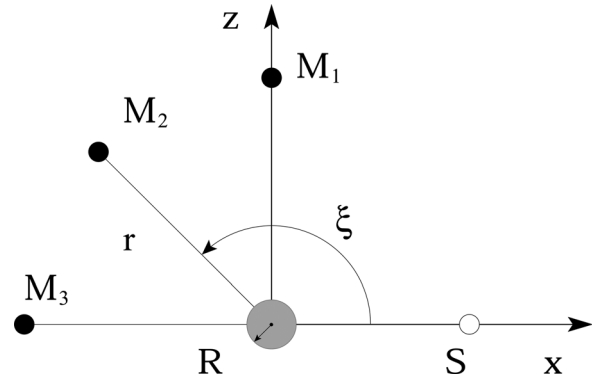


FIG. 3. Diffraction of acoustic waves generated by the source S by an impedance cylinder in 2-D or by an impedance sphere in 3-D. Three receivers M_1 , M_2 , and M_3 are located in the computational domain.

$$Z_L(\omega) = Z_M \coth(-ik_L d_L). \quad (30)$$

In the preceding equation, Z_M is the Miki impedance model of a semi-infinite ground layer, written as (Cotté et al., 2009)

$$Z_M = \left[1 + \mu \left(\frac{\sigma_0}{-i\omega} \right)^b \right], \quad (31)$$

with $\mu = 0.459$ and $b = 0.632$. The complex wave number in the porous layer k_L is similarly written in the form

$$k_L = \omega \left[1 + \nu \left(\frac{\sigma_0}{-i\omega} \right)^q \right], \quad (32)$$

with $\nu = 0.673$ and $q = 0.618$.

Three boundary conditions are considered: (1) a rigid ground, (2) a ground of finite impedance with $\sigma_0 = 120$ and $d_L = \infty$, which is denoted afterward by M120, and (3) a ground of finite impedance with $\sigma_0 = 12$ and $d_L = 0.2$, which is denoted afterward by M12L02.

A. 2-D test case: Acoustic scattering by an impedance cylinder

First, scattering by an impedance cylinder is considered. The coordinate transformation is defined by

$$x = (1 + \eta) \sin \zeta, \quad (33)$$

$$z = (1 + \eta) \cos \zeta. \quad (34)$$

Note that $(r = 1 + \eta, \zeta)$ correspond to the classical polar coordinates. The acoustic pressure is initialized by a Gaussian pulse centered at $(x_S, 0)$,

$$p(x, z, t = 0) = \exp \left[-\ln(2) \frac{(x - x_S)^2 + z^2}{B_x^2} \right], \quad (35)$$

where B_x is the Gaussian half-width set to $B_x = 0.4$. The abscissa of the source is set to $x_S = 8$ and three receivers denoted as M_1 , M_2 , and M_3 are placed in the computational domain with $r = 10$ and with, respectively, $\zeta = \pi/2$, $\zeta = 3\pi/4$, and $\zeta = \pi$.

The computational domain has 320 points in the ξ direction with a mesh size $\Delta\xi = 0.02$ and 201 points in the η direction with $\Delta\eta = 0.1$. Three thousand time iterations are performed. In the dimensionless form and with $c = 1$, the Courant–Friedrich–Lewy number reads $CFL = \Delta t / \Delta_{\min}$ where Δt is the time step and Δ_{\min} is the minimal spatial step. It is set to $CFL = 0.8$. For the boundaries, a periodic condition is imposed in the azimuthal direction and the radiation boundary condition of [Tam and Dong \(1996\)](#) is used in the radial direction. The reference point for the far-field formulation is chosen as the center of the cylinder.

In linear acoustics, propagation of an axisymmetric pressure pulse in free-field is equivalent to the propagation of a broadband point source ([Dragna et al., 2011](#)). The corresponding source strength $S(\omega)$ depends on the spatial distribution of the pulse. For the Gaussian pulse, it is written ([Dragna et al., 2011](#))

$$S(\omega) = i\omega\pi B^2 \exp\left(-\frac{\omega^2 B^2}{4}\right), \quad (36)$$

where $B = B_x / \sqrt{\ln 2}$. The source strength is the product of the 2-D spatial Fourier transform of the initial pressure distribution times the factor $i\omega$. For this diffraction problem, the analytical pressure in the time domain is then expressed as the following Fourier transform

$$p(r, \zeta, t) = \frac{1}{2\pi} \int_{-\infty}^{+\infty} S(\omega) \hat{p}(r, \zeta, \omega) \exp(-i\omega t) d\omega, \quad (37)$$

where $\hat{p}(r, \zeta, \omega)$ is the analytical solution of the problem for a point source in the frequency domain. It is divided into two terms $\hat{p} = \hat{p}_i + \hat{p}_d$. The incident pressure \hat{p}_i is the 2-D Green's function in free-field

$$\hat{p}_i = -\frac{i}{4} H_0^{(1)}\left(\omega \sqrt{r^2 + x_S^2 - 2rx_S \cos \zeta}\right). \quad (38)$$

The scattered pressure \hat{p}_d is written as

$$\hat{p}_d = -\frac{i}{4} \sum_{p=0}^{+\infty} C_p H_p^{(1)}(\omega x_S) H_p^{(1)}(\omega r) \cos p\zeta, \quad (39)$$

where the coefficients C_p are given by

$$C_p = -\epsilon_p \frac{J_{p+1}(\omega) - [p/\omega + i\beta] J_p(\omega)}{H_{p+1}^{(1)}(\omega) - [p/\omega + i\beta] H_p^{(1)}(\omega)}. \quad (40)$$

The term $\beta = 1/Z$ is the admittance and is null for a rigid ground. The parameter ϵ_p is equal to 1 for $p = 0$ and is equal to 2 otherwise. The derivation of the solution is detailed in [Appendix A](#).

[Figure 4](#) shows the pressure waveforms obtained at the receivers for the numerical and analytical solutions for the three boundary conditions and for the three defined angles. The first arrival for the cases $\zeta = \pi/2$ and $\zeta = 3\pi/4$ is the direct wave between the source and the receivers. Therefore it is identical for the three boundary conditions because it

does not depend on the boundary conditions. The other arrivals are the scattered waves. For the case $\zeta = \pi$, the different contributions do strongly overlap. In all cases, a very good agreement is found between the analytical and numerical waveforms.

B. 3-D test case: Acoustic scattering by an impedance sphere

To validate the proposed implementation for a 3-D geometry, a second test case dealing with diffraction of spherical waves by an impedance sphere is considered. It is a direct extension of the previous test case.

The following coordinate transformation is used:

$$x = (1 + \eta) \cos \xi, \quad (41)$$

$$y = (1 + \eta) \sin \zeta \sin \xi, \quad (42)$$

$$z = (1 + \eta) \cos \zeta \sin \xi. \quad (43)$$

Similarly, $(r = 1 + \eta, \zeta, \xi)$ correspond to the spherical coordinates, with the x axis as the polar axis. The acoustic source is a Gaussian pulse, centered at $(x_S, 0, 0)$ with $x_S = 3$. The Gaussian half width is $B_x = 0.4$. Three receivers denoted as M_1 , M_2 , and M_3 are placed in the computational domain with $r = 10$, $\zeta = 0$ and with, respectively, $\xi = \pi/2$, $\xi = 3\pi/4$, and $\xi = \pi$. Periodic boundary conditions are imposed in the polar and azimuthal directions, i.e., in the ξ and ζ directions. In the radial direction, i.e., in the η direction, the radiation boundary condition of [Bogey and Bailly \(2002\)](#) is used. The reference point for the far-field formulation is chosen as the center of the sphere. The Jacobian of the transformation

$$J = \frac{1}{(1 + \eta) \sin \xi}, \quad (44)$$

is singular at $\xi = 0$ and at $\xi = \pi$. To avoid these singularities, as proposed by [Mohseni and Colonius \(2000\)](#) for the polar case, the mesh is shifted by $\Delta\xi/2$ in the ξ direction. The method used for the discretization in the ξ direction is represented in [Fig. 5](#).

There are $160 \times 320 \times 600$ points used, respectively, in the ξ , ζ , and η directions with mesh sizes $\Delta\xi = \Delta\zeta = 0.02$ and $\Delta\eta = 0.025$. At the radial distance r and at the polar angle ξ , the azimuthal mesh spacing is $(r \sin \xi \Delta\zeta)$. Thus close to $\xi = 0$ and $\xi = \pi$, the mesh spacing is very small in the azimuthal direction compared to that at $\xi = \pi/2$. Because an explicit time-marching scheme is employed, this would result to a very small time step due to the CFL condition and, hence, to a large number of iterations. Following [Bogey et al. \(2011\)](#), the azimuthal spacing is artificially increased to avoid an important time step restriction near $\xi = 0$ and $\xi = \pi$. Thus instead of computing the finite differences from the adjacent points, they are determined from points separated by $(\Delta\xi)_{\text{eff}} = l\Delta\xi$, where $l \geq 1$ is an integer. The spatial derivative of the variable U in the ζ direction at point ζ_0 is then computed using the centered difference scheme over $2P + 1$ points

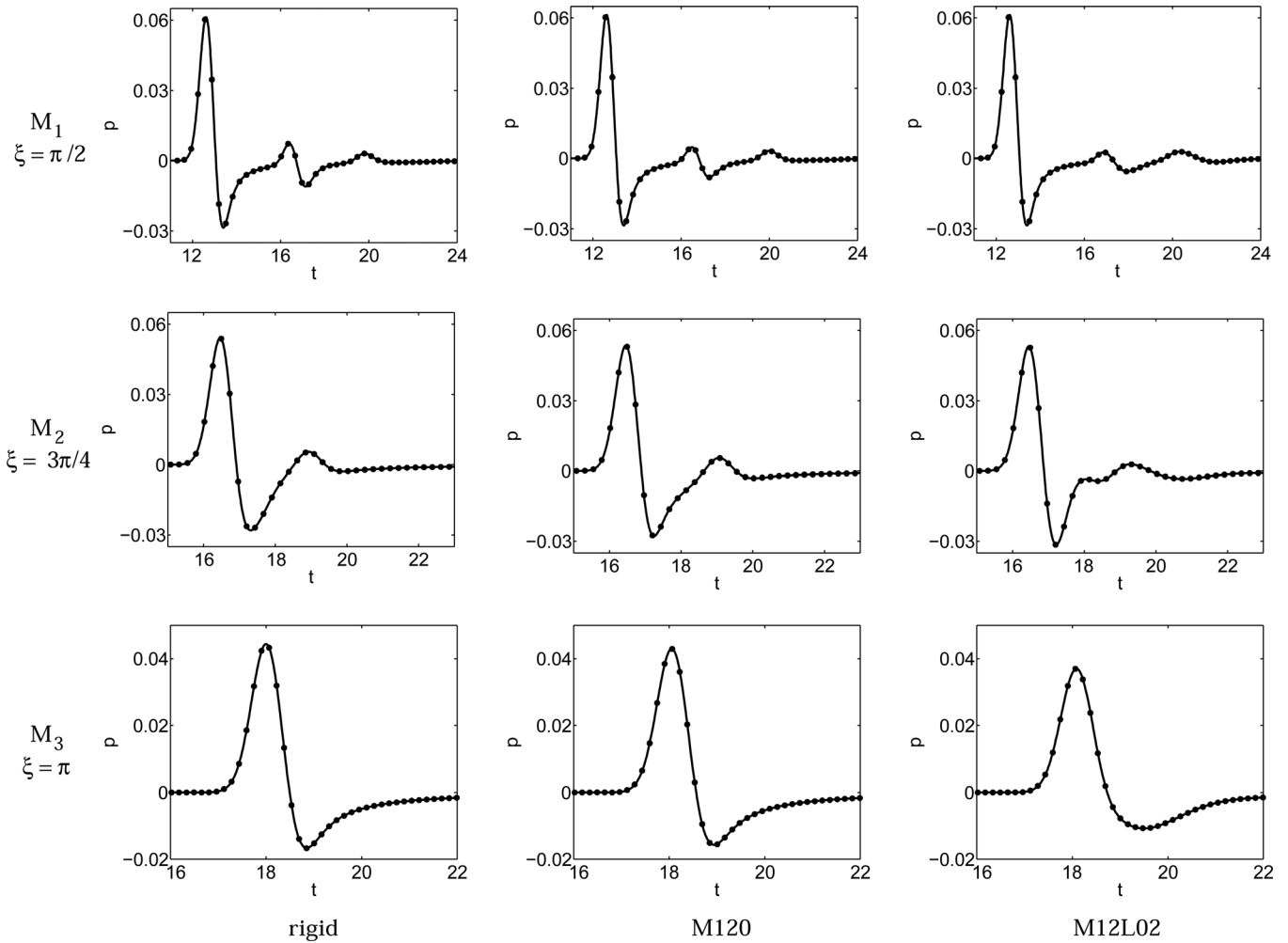


FIG. 4. Waveforms of the pressure obtained for the receivers M_1 , M_2 and M_3 and for the three boundary conditions versus time: Numerical (—) and analytical (●) solutions. The time and the pressure are made dimensionless by dividing them respectively by R/c_0 and $\rho_0 c_0^2$.

$$\frac{\partial U}{\partial \zeta}(\zeta_0) = \frac{1}{l\Delta\zeta} \sum_{m=-P}^P a_m U(\zeta_0 + lm\Delta\zeta), \quad (45)$$

where a_m are the stencil coefficients. Close to $\zeta = 0$ and $\zeta = \pi$, optimized second-order finite difference schemes over seven points proposed in [Bogey et al. \(2011\)](#) are employed in the ζ -direction with l between 2 and 40. Far from the poles, $l=1$, and fourth-order optimized finite-difference schemes over 11 points presented in [Sec. II B](#) are used. The effective mesh grid sizes ($r \sin \zeta (\Delta\zeta)_{\text{eff}}$) at radial distance $r=1$ are plotted versus ζ in [Fig. 6](#). The CFL condition is the most restrictive at the first and last points in the ζ direction. Thus at these points, $l=40$, and the effective mesh grid size in the ζ direction is 40 times larger than the actual one. This allows to increase the time step by a factor 40. Note also that, for a given r , the effective mesh spacing remains below $r\Delta\zeta$ for all values of ζ . Therefore it is expected that the accuracy is not affected by the reduced discretization. A schematic of the methods used for the computation of derivatives near the singularity is depicted in [Fig. 5](#).

Due to the azimuthal reduction, the finite-difference operator in the ζ direction depends on ζ . This implies that the finite-difference operator in the ζ direction does not

commute with the one in the ξ direction. The geometric conservation laws using formula proposed by [Vinokur and Yee \(2000\)](#) are not assured in this case. To eliminate the spurious waves, the strength of the selective filter is then increased to unity [see [Eq. \(12\)](#)]. The CFL number is set to 0.7, and 4500 time iterations are performed.

The analytical solution is written as the Fourier transform

$$p(r, \zeta, t) = \frac{1}{2\pi} \int_{-\infty}^{+\infty} S(\omega) \hat{p}(r, \zeta, \omega) \exp(-i\omega t) d\omega. \quad (46)$$

Because the problem is invariant in the azimuthal direction, the analytical solution does not depend on ζ . The source strength

$$S(\omega) = i\omega(\sqrt{\pi}B)^3 \exp\left(-\frac{\omega^2 B^2}{4}\right), \quad (47)$$

is the product of the 3-D spatial Fourier transform of the initial pressure distribution times the factor $i\omega$. The formula for the source strength can be easily deduced from the analytical solution of propagation of a Gaussian pressure pulse in free-field proposed by [Bogey and Bailly \(2002\)](#). The pressure in

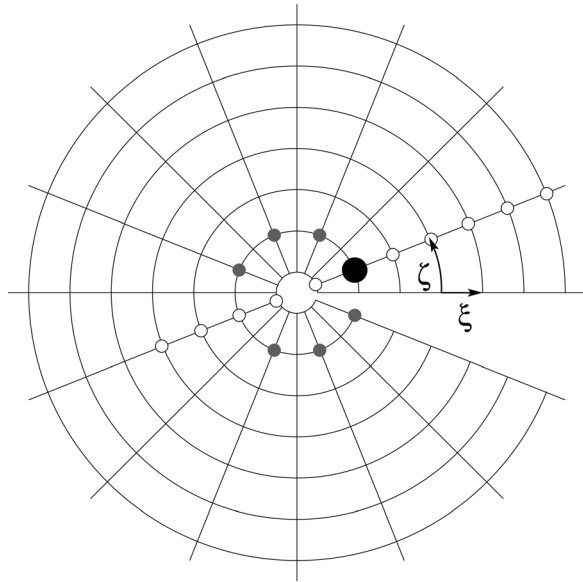


FIG. 5. Discretization near the singularity in a plane where η is constant at the grid point \bullet . The derivative is obtained from points \circ in the ξ -direction and from points \bullet in the ζ -direction with the reduced discretization method.

the frequency-domain for a point-source is still split as $\hat{p} = \hat{p}_i + \hat{p}_d$. The incident pressure is given by the 3-D Green's function

$$\hat{p}_i = -\frac{\exp\left(i\omega\sqrt{r^2 + x_S^2 - 2rx_S\cos\xi}\right)}{4\pi\sqrt{r^2 + x_S^2 - 2rx_S\cos\xi}}, \quad (48)$$

The scattered pressure \hat{p}_d is written as

$$\hat{p}_d = -\frac{i\omega}{4} \sum_{p=0}^{+\infty} B_p h_p^{(1)}(\omega x_S) h_p^{(1)}(\omega r) P_p(\cos\xi), \quad (49)$$

where the coefficients B_p are given by

$$B_p = -(2p+1) \frac{j_{p+1}(\omega) - [p/\omega + i\beta]j_p(\omega)}{h_{p+1}^{(1)}(\omega) - [p/\omega + i\beta]h_p^{(1)}(\omega)}. \quad (50)$$

In the preceding equations, j_p , h_p , and P_p are, respectively, the spherical Bessel function of the first kind and the

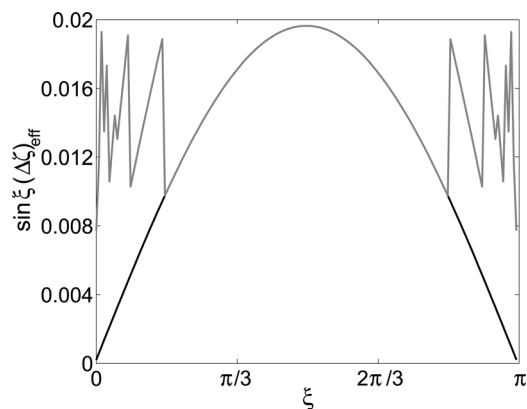


FIG. 6. Mesh grid size in the azimuthal direction as a function of ξ for the 3-D test case: Without (—) and with (---) reduced azimuthal discretization.

spherical Hankel function of order p and the Legendre polynomial of degree p . The derivation of the solution is briefly described in Appendix B.

In Fig. 7, the pressure waveforms obtained at the three receivers for the three boundary conditions are represented. In all cases, an almost perfect agreement is found between the analytical and numerical solutions. Therefore it is shown that the boundary conditions proposed in this study are well adapted to time-domain methods.

IV. ILLUSTRATION: DIFFRACTION DUE TO TOPOGRAPHY

In this last section, acoustic propagation above an embankment with different meteorological conditions is examined. This example aims at studying efficiency of a noise embankment close to a highway. The topography of the site is represented in Fig. 8. The embankment is 2 m high and 9 m thick. The coordinate transformation is defined by

$$x = \xi, \quad (51)$$

$$y = \zeta, \quad (52)$$

$$z = \eta + H(\xi, \zeta), \quad (53)$$

where H is the ground profile. In this case, the curvilinear coordinate η corresponds to the height above the ground. In the x direction, quadratic splines are used to fit the desired ground profile. In the y direction, the profile is modulated by a Gaussian profile the half width of which is equal to $B_y = 15$ m. The ground profile is then expressed as

$$H(x, y) = \exp\left(-\ln(2)\frac{y^2}{B_y^2}\right) (a_2x^2 + a_1x + a_0), \quad (54)$$

where numerical parameters are given in Table I.

As done in Sec. III B, the initial disturbances are a pressure Gaussian pulse with a half width $B_x = 0.15$ m. It is centered at $x_S = 0$ m, $y_S = 0$ m, and $z_S = 0.5$ m. It must be pointed out that this example aims at illustrating the possibilities of the solver. Thus this type of source is not realistic for highway traffic noise. An incoherent line source (see, e.g., Salomons, 2001) with typical spectrum and directivity of transportation noise would be more representative. Three different surface impedances are used. Up to $x = 2$ m, the road is modeled by a rigid surface. From $x = 2$ m to $x = 13$ m including the embankment, a grassy ground is considered with the Miki impedance model of a semi-infinite ground layer of air flow resistivity $\sigma_0 = 100$ kPa s m^{-2} . Then from $x = 13$ m, the Miki impedance model of a rigidly backed layer of air flow resistivity $\sigma_0 = 300$ kPa s m^{-2} and of thickness $d_L = 0.02$ m is used to model a typical field. At the other boundaries, the radiation boundary condition of Bogey and Bailly (2002) is employed. The reference point for the far-field formulation is located on the ground and at the source position, i.e., at $(x = 0$ m, $y = 0$ m, $z = 0$ m).

To study the influence of a velocity gradient on the sound propagation, a logarithmic velocity profile is considered

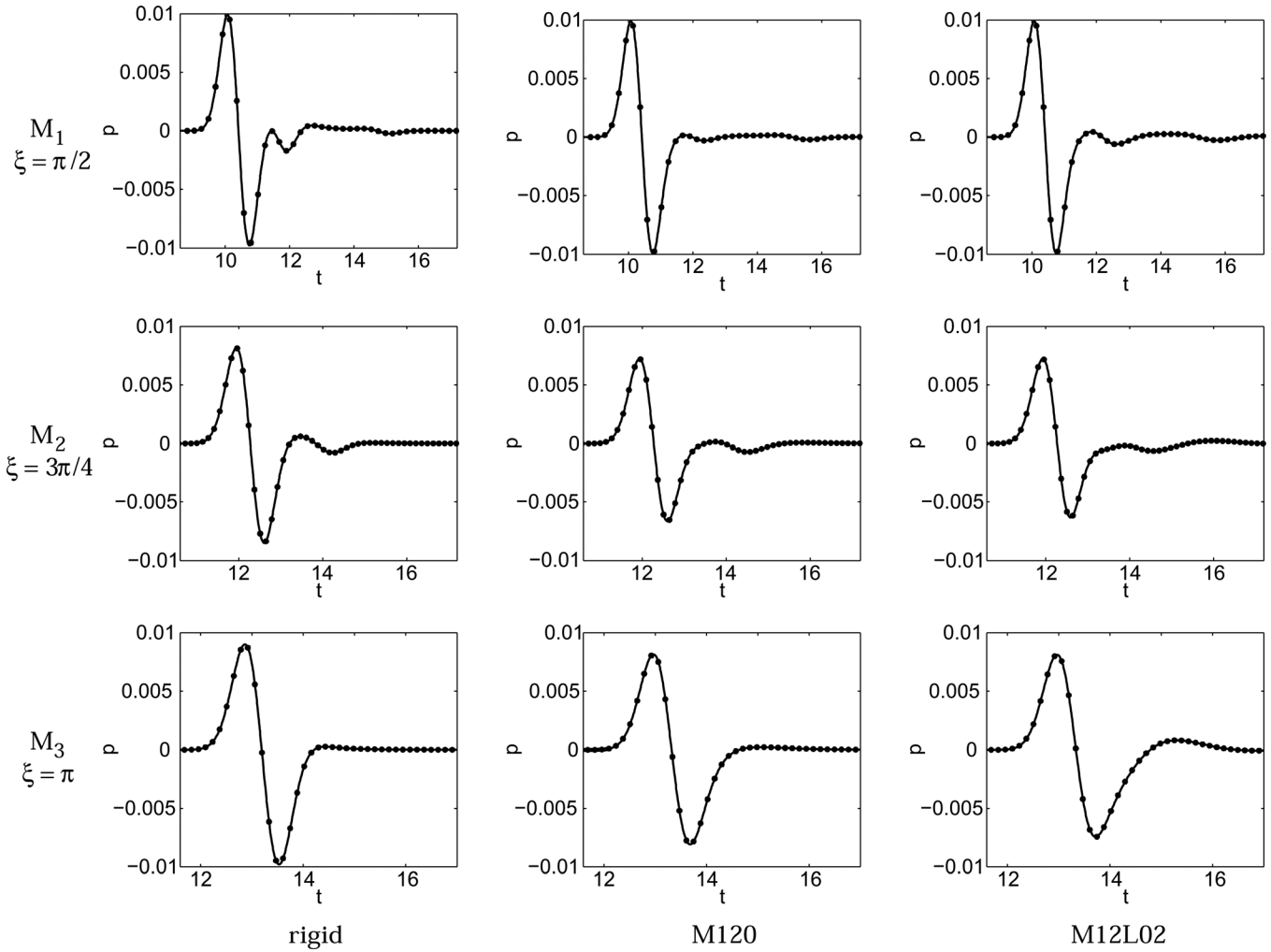


FIG. 7. Waveforms of the pressure obtained for the receivers M_1 , M_2 and M_3 and for the three boundary conditions versus time: Numerical (—) and analytical (●) solutions. The time and the pressure are made dimensionless by dividing them respectively by R/c_0 and $\rho_0 c_0^2$.

$$\mathbf{V}_0(z) = a_c \ln \frac{\eta + z_0}{z_0} (\cos\theta \mathbf{e}_x + \sin\theta \mathbf{e}_y), \quad (55)$$

where the roughness length is chosen as $z_0 = 0.1$ m. The parameter a_c is set to 0 m s^{-1} for no wind condition and to 2 m s^{-1} otherwise. Five configurations are considered. First, influence of the embankment on the sound pressure level is

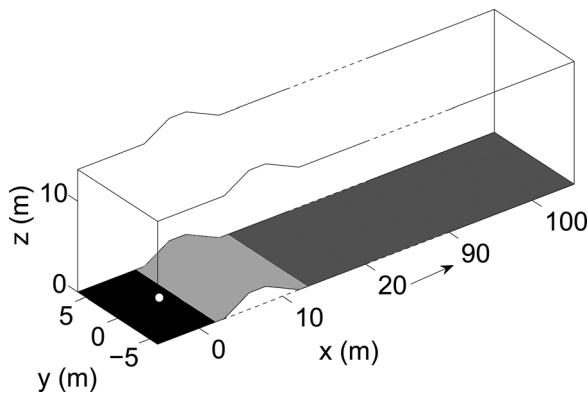


FIG. 8. Schematic of the computational domain. Each color denotes a different ground surface impedance. The source position is represented by the white dot.

studied. In the first two computations, propagation of acoustic waves over the site with and without the embankment is examined in a homogeneous atmosphere. Then influence of the meteorological effects on the efficiency of the embankment are taken into account by investigating three wind directions: Downwind condition with $\theta = 0$, upwind condition with $\theta = \pi$, and transverse wind condition with $\theta = \pi/2$.

The numerical domain is $[-5 \text{ m}; 105 \text{ m}] \times [-6.25 \text{ m}; 6.25 \text{ m}] \times [0 \text{ m}; 13.5 \text{ m}]$, with a uniform mesh size $\Delta\xi$

TABLE I. Numerical parameters used to define the ground profile in Eq. (54).

$x, \text{ m}$	$a_2, \text{ m}^{-1}$	a_1	$a_0, \text{ m}$
$-5.0 \rightarrow 2.85$	0.0	0.0	0.0
$2.85 \rightarrow 3.15$	1.111×10^0	-6.333×10^0	9.025×10^0
$3.15 \rightarrow 5.85$	0.0	6.666×10^{-1}	-2.0
$5.85 \rightarrow 6.15$	-1.111×10^0	1.366×10^1	-4.003×10^1
$6.15 \rightarrow 7.85$	0.0	0.0	2.0
$7.85 \rightarrow 8.15$	-8.333×10^{-1}	1.308×10^1	-4.935×10^1
$8.15 \rightarrow 11.85$	0.0	-0.5	6.0
$11.85 \rightarrow 12.15$	8.333×10^{-1}	-2.025×10^1	1.230×10^2
$12.15 \rightarrow 105.0$	0.0	0.0	0.0

$= \Delta\zeta = \Delta\eta = 0.05$ m. There are about 15×10^6 points. The CFL number is set to 0.7, and 3200 time iterations are performed so that the pulse leaves the computational domain.

Waveforms obtained at a receiver at $x = 100$ m, $y = 0$ m, and $z = 2$ m for the five computations are represented in Fig. 9. First, note that the arrival time obtained for the case with the embankment in a homogeneous atmosphere is slightly greater to that obtained without embankment, about $\Delta t = 0.7$ ms, because of the path difference due to the embankment height. The total sound pressure level

$$Lp = 10 \log_{10} \left[\int_{-\infty}^{+\infty} \frac{p^2(t)}{p_{\text{ref}}^2} dt \right], \quad (56)$$

where p_{ref} is a reference pressure is 7 dB lower. This shows that for this particular source, the embankment is effective to reduce the broadband sound pressure level. In downwind condition, multiple arrivals can be distinguished on the waveform. The arrival time is smaller than that in no wind condition because the effective sound speed is greater. As expected, downwind condition causes an increase of the total sound pressure level by 5 dB. In the upwind condition, the effective sound speed is smaller than the ambient sound speed. Therefore the arrival time is larger. Furthermore, the total sound pressure level is reduced by 8.6 dB. Finally, comparably to other computations performed by Salomons (2001), transverse wind has no effect. Indeed the difference on the total sound pressure level compared to no wind condition is only of 0.1 dB.

To evaluate the effect of the embankment in the frequency domain, the insertion loss is introduced by the relation

$$IL(f) = 20 \log_{10} \left| \frac{\hat{p}(f)}{\hat{p}_{w/o}(f)} \right|, \quad (57)$$

where $\hat{p}(f)$ is the Fourier transform of the pressure and $\hat{p}_{w/o}(f)$ is the corresponding value for the configuration without embankment in no wind condition. The insertion

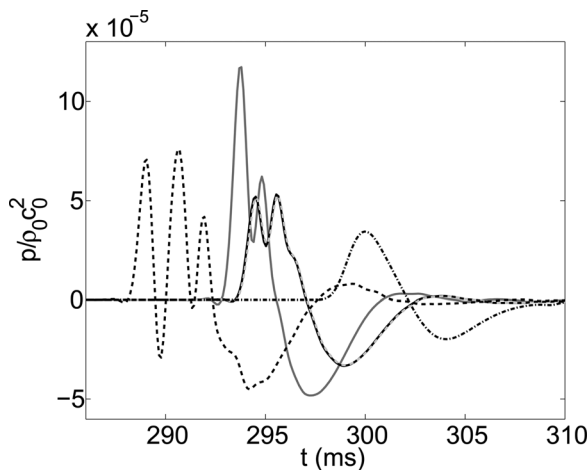


FIG. 9. Waveforms at a receiver at $x = 100$ m, $y = 0$ m, and $z = 2$ m for no wind condition (—), downwind condition (---), upwind condition (-.-), transverse wind condition (·-·), and no wind condition (—) without embankment.

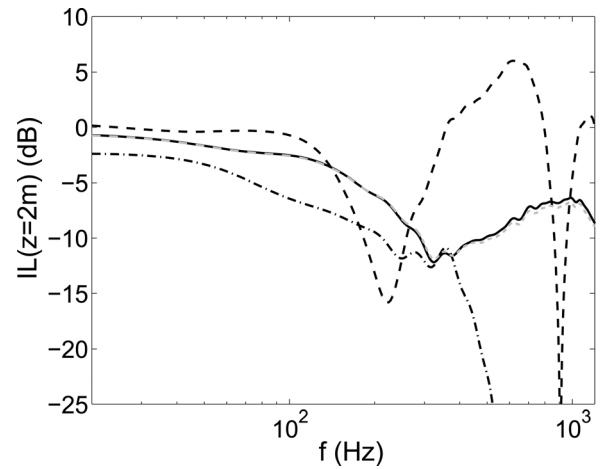


FIG. 10. Insertion loss versus frequency at a receiver at $x = 100$ m, $y = 0$ m, and $z = 2$ m for no wind condition (—), downwind condition (---), upwind condition (-.-), and transverse wind condition (·-·).

loss at a receiver located at $x = 100$ m, $y = 0$ m, and $z = 2$ m is plotted versus frequency in Fig. 10. The embankment enables to reduce the sound pressure level over all the frequency range. In the upwind condition, high frequencies are significantly attenuated, and the efficiency of the embankment is dramatically increased for frequencies larger than 400 Hz. The downwind condition causes an increase of the sound pressure level for high frequencies. Around $f = 800$ Hz, the insertion loss becomes positive, which means that the sound

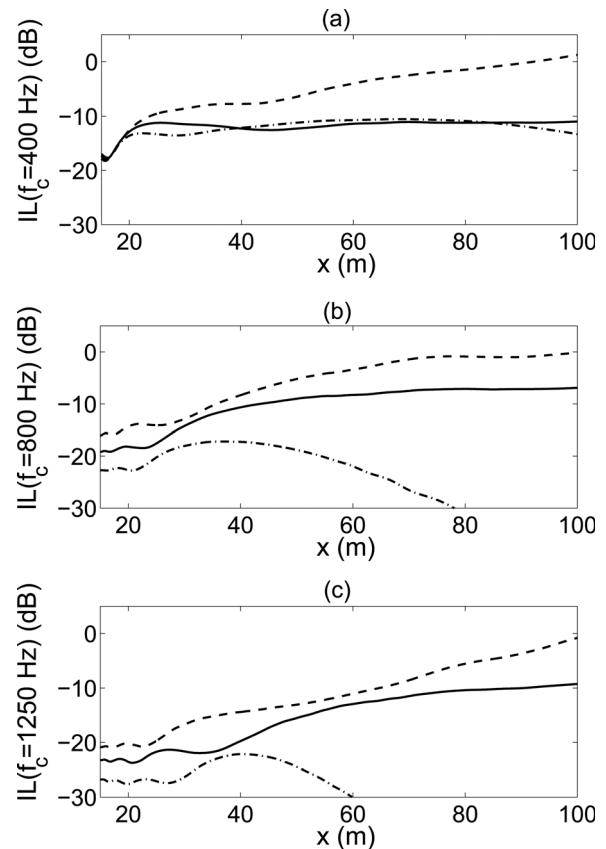


FIG. 11. Insertion loss for receivers at $y = 0$ m and $z = 2$ m versus abscissa x for 1/3-octave bands centered at (a) 400 Hz, (b) 800 Hz and (c) 1250 Hz and for no wind condition (—), downwind condition (---), and upwind condition (-.-).

pressure level is higher than without embankment in no-wind conditions.

The evolution of the insertion loss with x is now investigated. It is shown in Fig. 11 for a line of receivers located behind the embankment at $y = 0$ m and $z = 2$ m and for different 1/3-octave bands. The case of the transverse wind is not represented because it is similar to the no-wind condition. For receiver just behind the embankment, the insertion loss is very large, i.e., around 20 dB. In the no-wind condition, the efficiency decreases with increasing x depending on the frequency. At high frequencies $f > 400$ Hz, influence of the meteorological conditions on the insertion loss is significant from $x = 20$ m. At lower frequencies $f < 400$ Hz, it is visible at larger distance (5 dB difference from $x = 40$ m between the insertion loss in downwind and no-wind conditions). In downwind condition, acoustic energy is refracted to the ground. Therefore the embankment efficiency decreases with increasing x and also with increasing frequency. In upwind condition, the insertion loss decreases rapidly once the receiver is in the shadow zone. Thus for $f = 1250$ Hz, more than 15 dB difference between the insertion loss in upwind and no-wind conditions is obtained for $x > 60$ m.

V. CONCLUSION

In this paper, a time-domain numerical propagation solver using optimized high-order finite-difference schemes has been developed on the basis of the linearized Euler equations. Meteorological and ground effects have been both taken into account. Topography has been accounted for by using curvilinear coordinates. A time-domain impedance boundary condition recently proposed has been extended for non-flat terrain profiles. It has been validated against two diffraction test-cases in 2-D and 3-D geometries. In both case, an excellent agreement has been obtained between the analytical and numerical solutions. The capabilities of the solver have been then illustrated with a typical outdoor sound propagation problem dealing with propagation above an embankment and above mixed ground impedance surfaces in a heterogeneous medium. It can also be noted that curvilinear transformation is applicable for any continuous coordinate transformation. In particular, it is useful for coupling with meteorological models (such as micro-meteorological models using large eddy simulations). Indeed, computation of the acoustic propagation can be performed on the same grid without requiring interpolation of the meteorological data to the grid of the acoustic solver; this is something that can be time-consuming especially for 3-D problems. Moreover, it can be applied to terrains with large slope angle ($>45^\circ$), such as steep-sided valleys, for which terrain-following coordinate transformations are not relevant.

Future work will focus on the modeling of realistic sources for transportation noise applications. In particular, coupled effects of a moving source and of a complex site on the acoustic pressure field will be studied.

ACKNOWLEDGMENTS

Support by CNRS and SNCF is gratefully acknowledged. This work was granted access to the HPC resources

of IDRIS under the allocation 2011-022203 made by Grand Equipement National de Calcul Intensif (GENCI). It was conducted in the framework of the LabEx CeLyA (Centre Lyonnais d'Acoustique, ANR-10-LABX-60). The authors would like to thank O. Marsden and C. Bogey for helpful discussions.

APPENDIX A: ANALYTICAL SOLUTION FOR DIFFRACTION OF CYLINDRICAL WAVES BY AN IMPEDANCE CYLINDER

This appendix details the derivation of the analytical solution for propagation of acoustic waves from a point source placed above an impedance cylinder in a 2-D geometry. The cylinder radius is denoted as $R = 1$. The point source and the receiver are located, respectively, at $\mathbf{r}_S = (x_S, 0)$ and at $\mathbf{r} = (x_R, z_R)$. Their respective polar coordinates are $\mathbf{r}_S = (r_S, 0)$ and $\mathbf{r} = (r, \theta)$. The surface of the cylinder is characterized by its admittance denoted as β . The acoustic pressure $\hat{p}(r, \theta, \omega)$ satisfies the Helmholtz equation in polar coordinates

$$\frac{1}{r} \frac{\partial}{\partial r} \left(r \frac{\partial \hat{p}}{\partial r} \right) + \frac{1}{r^2} \frac{\partial^2 \hat{p}}{\partial \theta^2} + \omega^2 \hat{p} = \delta(x - x_S) \delta(z), \quad (\text{A1})$$

with the Sommerfeld condition at infinity and the impedance boundary condition on the cylinder

$$\left. \frac{\partial \hat{p}}{\partial r} \right|_R + i\omega\beta \hat{p}(R, \theta) = 0. \quad (\text{A2})$$

The pressure is split into two components $\hat{p}(r, \theta, \omega) = \hat{p}_i(r, \theta, \omega) + \hat{p}_d(r, \theta, \omega)$ where \hat{p}_i is the incident pressure on the cylinder and \hat{p}_d the scattered pressure due to the cylinder. The incident pressure \hat{p}_i is given by the 2-D Green's function in free-field

$$\hat{p}_i(r, \theta) = -\frac{i}{4} H_0^{(1)}(\omega |\mathbf{r} - \mathbf{r}_S|). \quad (\text{A3})$$

Using the addition theorem (Gradshteyn and Ryzhik, 1980), the incident pressure is rewritten as

$$\hat{p}_i(r, \theta) = -\frac{i}{4} \sum_{p=0}^{+\infty} \epsilon_p H_p^{(1)}(\omega r_>) J_p(\omega r_<) \cos p\theta, \quad (\text{A4})$$

with $r_> = \max(r_S, r)$ and $r_< = \min(r_S, r)$. The parameter ϵ_p is equal to 1 for $p = 0$ and is equal to 2 otherwise.

Using the separation of variables method and accounting for the symmetry over x axis and the Sommerfeld condition, the scattered pressure is sought in the form

$$\hat{p}_d(r, \theta) = -\frac{i}{4} \sum_{p=0}^{+\infty} C_p H_p^{(1)}(\omega x_S) H_p^{(1)}(\omega r) \cos p\theta. \quad (\text{A5})$$

The coefficients C_p are obtained by using the impedance boundary condition

$$\left. \frac{\partial \hat{p}_d}{\partial r} \right|_R + i\omega\beta \hat{p}_d(R, \theta) = -\left. \frac{\partial \hat{p}_i}{\partial r} \right|_R - i\omega\beta \hat{p}_i(R, \theta). \quad (\text{A6})$$

To do so, the normal derivative of the scattered pressure on the cylinder is calculated with

$$\frac{\partial \hat{p}_d}{\partial r} \Big|_R = -i \frac{\omega}{4} \sum_{p=0}^{+\infty} C_p H_p^{(1)}(\omega x_S) \times \cos p \theta \frac{H_{p-1}^{(1)}(\omega R) - H_{p+1}^{(1)}(\omega R)}{2}. \quad (\text{A7})$$

Using the following formula for the Hankel function:

$$H_{p-1}^{(1)}(z) + H_{p+1}^{(1)}(z) = \frac{2p}{z} H_p^{(1)}(z), \quad (\text{A8})$$

yields

$$\frac{\partial \hat{p}_d}{\partial r} \Big|_R = -\frac{i}{4} \omega \sum_{p=0}^{+\infty} C_p H_p^{(1)}(\omega x_S) \times \cos p \theta \left(\frac{p}{\omega R} H_p^{(1)}(\omega R) - H_{p+1}^{(1)}(\omega R) \right). \quad (\text{A9})$$

If one adds $i\omega\beta\hat{p}_d$, one finally gets the equation

$$\frac{\partial \hat{p}_d}{\partial r} \Big|_R + i\omega\beta\hat{p}_d(R, \theta) = -\frac{i}{4} \omega \sum_{p=0}^{+\infty} C_p H_p^{(1)}(\omega x_S) \times \cos p \theta \left(\left[\frac{p}{\omega R} + i\beta \right] H_p^{(1)}(\omega R) - H_{p+1}^{(1)}(\omega R) \right). \quad (\text{A10})$$

The same procedure is applied for the incident pressure, which yields

$$-\frac{\partial \hat{p}_i}{\partial r} \Big|_R - i\omega\beta\hat{p}_i(R, \theta) = -\frac{i}{4} \omega \sum_{p=0}^{+\infty} -\epsilon_p H_p^{(1)}(\omega x_S) \cos p \theta \times \left(\left[\frac{p}{\omega R} + i\beta \right] J_p(\omega R) - J_{p+1}(\omega R) \right). \quad (\text{A11})$$

Finally, the expression for the coefficients C_p is obtained by matching the series term in Eqs. (A10) and (A11):

$$C_p = -\epsilon_p \frac{J_{p+1}(\omega R) - [p/\omega R + i\beta] J_p(\omega R)}{H_{p+1}^{(1)}(\omega R) - [p/\omega R + i\beta] H_p^{(1)}(\omega R)}. \quad (\text{A12})$$

To summarize, the pressure $\hat{p}(r, \theta, \omega)$ is computed from Eqs. (A3) and (A5). The coefficients C_p are given in the preceding equation.

APPENDIX B: ANALYTICAL SOLUTION FOR DIFFRACTION OF SPHERICAL WAVES BY AN IMPEDANCE SPHERE

This appendix describes the derivation of the analytical solution for diffraction of spherical waves by an impedance sphere. The calculation is very close to that of diffraction

of cylindrical waves by an impedance cylinder, detailed in Appendix A. The sphere radius is expressed as $R = 1$. The point source and the receiver are located respectively at $\mathbf{r}_S = (x_S, 0, 0)$ and at $\mathbf{r} = (x_R, 0, z_R)$. The corresponding spherical coordinates $\mathbf{r}_S = (r_S, 0, 0)$ and $\mathbf{r} = (r, \theta, \phi)$ are also employed. Because the problem is invariant in the ϕ direction, the azimuthal angle is set to $\phi = 0$ without loss of generality. The surface of the sphere is characterized by its admittance denoted as β . The acoustic pressure $\hat{p}(r, \theta, \omega)$ satisfies the Helmholtz equation in spherical coordinates

$$\frac{1}{r^2} \frac{\partial}{\partial r} \left(r^2 \frac{\partial \hat{p}}{\partial r} \right) + \frac{1}{r^2 \sin \theta} \frac{\partial}{\partial \theta} \left(\sin \theta \frac{\partial \hat{p}}{\partial \theta} \right) + \omega^2 \hat{p} = \delta(x - x_S) \delta(y) \delta(z), \quad (\text{B1})$$

with the Sommerfeld condition at infinity and with the impedance boundary condition on the sphere surface.

As done in Appendix A, the pressure is split into the incident pressure on the sphere \hat{p}_i and the scattered pressure due to the sphere \hat{p}_d . The incident pressure \hat{p}_i is given by the 3-D Green's function in free-field

$$\hat{p}_i(r, \theta) = -\frac{\exp(i\omega |\mathbf{r} - \mathbf{r}_S|)}{4\pi |\mathbf{r} - \mathbf{r}_S|}. \quad (\text{B2})$$

An other addition theorem (Gradshteyn and Ryzhik, 1980) allows one to write

$$\hat{p}_i(r, \theta) = -\frac{i\omega}{4\pi} \sum_{p=0}^{+\infty} (2p+1) h_p^{(1)}(\omega r_{>}) j_p(\omega r_{<}) P_p(\cos \theta), \quad (\text{B3})$$

with $r_{>} = \max(r_S, r)$ and $r_{<} = \min(r_S, r)$.

Due to the symmetry over x axis and to the Sommerfeld condition, the scattered pressure is written as

$$\hat{p}_d(r, \theta) = -\frac{i\omega}{4} \sum_{p=0}^{+\infty} B_p h_p^{(1)}(\omega x_S) h_p^{(1)}(\omega r) P_p(\cos \theta). \quad (\text{B4})$$

Using the impedance boundary condition on the sphere surface and applying the formula for the spherical Bessel and Hankel function

$$h_{p-1}^{(1)}(z) + h_{p+1}^{(1)}(z) = \frac{2p+1}{z} h_p^{(1)}(z), \quad (\text{B5})$$

leads to the following expression for the coefficients B_p :

$$B_p = -(2p+1) \frac{j_{p+1}(\omega R) - [p/\omega R + i\beta] j_p(\omega R)}{h_{p+1}^{(1)}(\omega R) - [p/\omega R + i\beta] h_p^{(1)}(\omega R)}. \quad (\text{B6})$$

The acoustic pressure $\hat{p}(r, \theta, \omega)$ is computed from Eqs. (B2) and (B4). The coefficients B_p are given in the preceding equation.

- Attenborough, K. (2002). "Sound propagation close to the ground," *Annu. Rev. Fluid Mech.* **34**, 51–82.
- Berland, J., Bogey, C., and Bailly, C. (2006). "Low-dissipation and low-dispersion fourth-order Runge–Kutta algorithm," *Comput. Fluids* **35**, 1459–1463.
- Berland, J., Bogey, C., Marsden, O., and Bailly, C. (2007). "High order, low dispersive and low dissipative explicit schemes for multiple-scale and boundary problems," *J. Comp. Phys.* **224**, 637–662.
- Blairon, N., Blanc-Benon, P., Bérenghier, M., and Juvé, D. (2002). "Outdoor sound propagation in complex environments: Experimental validation of a PE approach," in *Tenth Long Range Sound Propagation Symposium*, Grenoble, France, pp. 114–128, <http://ncpa.olemiss.edu/long-range-sound-propagation-lrsp/> (Last viewed 1/14/2013).
- Blumrich, R., and Heimann, D. (2002). "A linearized Eulerian sound propagation model for studies of complex meteorological effects," *J. Acoust. Soc. Am.* **112**, 446–455.
- Bogey, C., and Bailly, C. (2002). "Three-dimensional non-reflective boundary conditions for acoustic simulations: Far-field formulation and validation test cases," *Acta Acust. Acust.* **88**, 463–471.
- Bogey, C., and Bailly, C. (2004). "A family of low dispersive and low dissipative explicit schemes for flow and noise computations," *J. Comp. Phys.* **194**, 194–214.
- Bogey, C., de Cacqueray, N., and Bailly, C. (2009). "A shock-capturing methodology based on adaptive spatial filtering for high-order non-linear computations," *J. Comp. Phys.* **228**, 1447–1465.
- Bogey, C., de Cacqueray, N., and Bailly, C. (2011). "Finite differences for coarse azimuthal discretization and for reduction of effective resolution near origin of cylindrical flow equations" *J. Comp. Phys.* **230**, 1134–1146.
- Collins, M. D. (1990). "The rotated parabolic equation and the sloping ocean bottoms," *J. Acoust. Soc. Am.* **87**, 1035–1037.
- Cotté, B., Blanc-Benon, P., Bogey, C., and Poisson, F. (2009). "Time-domain impedance boundary conditions for simulations of outdoor sound propagation," *AIAA J.* **47**, 2391–2403.
- Dragna, D., Cotté, B., Blanc-Benon, P., and Poisson, F. (2011). "Time-domain simulations of outdoor sound propagation with suitable impedance boundary conditions," *AIAA J.* **49**, 1420–1428.
- Guillaume, G., Picaut, J., Dutilleul, G., and Gauvreau, B. (2011). "Time-domain impedance formulation for transmission line matrix modeling of outdoor sound propagation," *J. Sound Vib.* **330**, 6467–6481.
- Gradshteyn, I. S., and Ryzhik, I. M. (1980). *Table of Integrals, Series, and Products*, 4th ed. (Academic, New York), p. 979, item 8.531, formula 2, and p. 980, item 8.533, formula 1.
- Heimann, D., and Karle, R. (2006). "A linearized Euler finite-difference time-domain sound propagation model with terrain-following coordinates," *J. Acoust. Soc. Am.* **119**, 3813–3821.
- Hornikx, M., Waxler, R., and Forssén, J. (2010). "The extended Fourier pseudospectral time-domain method for atmospheric sound propagation," *J. Acoust. Soc. Am.* **128**, 1632–1646.
- Jean, P. (1998). "A variational approach for the study of outdoor sound propagation and application to railway noise," *J. Sound Vib.* **212**, 275–294.
- Jensen, F. B., Kuperman, W. A., Porter, M. B., and Schmidt, H. (1994). *Computational Ocean Acoustics* (AIP, Melville, NY), pp. 352–357.
- Kurbatskii, K. A., and Tam, C. K. W. (1997). "Cartesian boundary treatment of curved walls for high-order computational aeroacoustics schemes," *AIAA J.* **35**, 133–140.
- Lihoreau, B., Gauvreau, B., Bérenghier, M., Blanc-Benon, P., and Calmet, I. (2006). "Outdoor sound propagation modeling in realistic environments: Application of coupled parabolic and atmospheric models." *J. Acoust. Soc. Am.* **120**, 110–119.
- Luebbers, R. J., and Hunsberger, F. (1992). "FDTD for Nth-order dispersive media," *IEEE Trans. Antennas Propag.* **40**, 1297–1301.
- Marsden, O. (2005). "Calcul direct du rayonnement acoustique de profils par une approche curviligne d'ordre élevé" ("Direct noise computation of aerofoils by a high-order curvilinear approach"), Ph.D. thesis, École Centrale de Lyon, No. 2005-47.
- Marsden, O., Bogey, C., and Bailly, C. (2005). "High-order curvilinear simulations of flows around non-Cartesian bodies," *J. Comp. Acoust.* **13**, 731–748.
- Mesbah, M., Meyers, J., and Baelmans, M. (2008). "Acoustic performance of nonreflecting boundary conditions for a range of incident angles," *J. Comp. Acoust.* **16**, 11–29.
- Miki, Y. (1990). "Acoustical properties of porous materials—modifications of Delany–Bazley models," *J. Acoust. Soc. Jpn.* **11**, 19–24.
- Mohseni, K., and Colonius, T. (2000). "Numerical treatment of polar coordinate singularities," *J. Comp. Phys.* **157**, 787–795.
- Ostashev, V. E., Collier, S. L., Wilson, D. K., Aldridge, D. F., Symons, N. P., and Marlin, D. (2007). "Padé approximation in time-domain boundary conditions of porous surfaces," *J. Acoust. Soc. Am.* **122**, 107–112.
- Ostashev, V. E., Wilson, D. K., Liu, L., Aldridge, D. F., Symons, N. P., and Marlin, D. (2005). "Equations for finite-difference, time-domain simulation of sound propagation in moving inhomogeneous media and numerical implementation," *J. Acoust. Soc. Am.* **117**, 503–517.
- Özyörük, Y., and Long, L. N. (1996). "A time-domain implementation of surface acoustic impedance condition with and without flow," in *Second AIAA/CEAS Aeroacoustics Conference*, State College, PA, AIAA Paper No. 96-1663.
- Parakkal, S., Gilbert, K. E., and Di, X. (2012). "Application of the Beiliss–Tappert parabolic equation method to sound propagation over irregular terrain," *J. Acoust. Soc. Am.* **131**, 1039–1046.
- Parakkal, S., Gilbert, K. E., Di, X., and Bass, H. E. (2010). "A generalized polar coordinate method for sound propagation over large-scale irregular terrain," *J. Acoust. Soc. Am.* **128**, 2573–2580.
- Premat, E., and Gabillet, Y. (2000). "A new boundary-element method for predicting outdoor sound propagation and application to the case of a sound barrier in the presence of downward refraction," *J. Acoust. Soc. Am.* **108**, 2775–2783.
- Reymen, Y., Baelmans, M., and Desmet, W. (2006). "Time-Domain Impedance Formulation based on Recursive Convolution," in *Twelfth AIAA/CEAS Aeroacoustics Conference*, Cambridge, MA, AIAA Paper No. 2006-2685.
- Rienstra, S. W. (1988). "1-D reflection at an impedance wall," *J. Sound Vib.* **125**, 43–51.
- Sack, R. A., and West, M. (1995). "A parabolic equation for sound propagation in two dimensions over any smooth terrain profile: The generalized terrain parabolic equation (GT-PE)," *Appl. Acoust.* **45**, 113–129.
- Salomons, E. (2001). *Computational Atmospheric Acoustics* (Kluwer Academic Publishers, Dordrecht), pp. 30 and 53–56.
- Salomons, E. M., Blumrich, R., and Heimann, D. (2002). "Eulerian time-domain model for sound propagation over a finite-impedance ground surface. Comparison with frequency-domain models," *Acta Acust. Acust.* **88**, 483–492.
- Tam, C. K. W., and Dong, Z. (1996). "Radiation and outflow boundary conditions for direct computation of acoustic and flow disturbances in a non-uniform mean flow," *J. Comp. Acoust.* **4**, 175–201.
- Tam, C. K. W., and Hardin, J. C. (1997). *Second Computational AeroAcoustics (CAA) Workshop on Benchmark Problems*, Publication No. 3352, Icase/NASA (National Aeronautics and Space Administration Conference), pp. 1–14.
- Van Renterghem, T., and Botteldooren, D. (2003). "Numerical simulation of the effect of trees on downwind noise barrier performance," *Acta Acust. Acust.* **89**, 764–778.
- Vinokur, M., and Yee, H. C. (2000). "Extension of efficient low dissipation high-order schemes for 3-D curvilinear moving grids," NASA Technical Report TM 2000-209598 (National Aeronautics and Space Administration, Washington, DC).
- Visbal, M. R., and Gaitonde, D. V. (2002). "On the use of higher-order finite-difference schemes on curvilinear and deforming meshes," *J. Comp. Phys.* **181**, 155–185.
- Wilson, D. K., Ostashev, V. E., Collier, S. L., Symons, N. P., Aldridge, D. F., and Marlin, D. H. (2007). "Time-domain calculations of sound interactions with outdoor ground surfaces," *Appl. Acoust.* **68**, 173–200.